Available online at www.sciencedirect.com

SciVerse ScienceDirect

Photonics and Nanostructures – Fundamentals and Applications 11 (2013) 15–28

PHOTONICS AND NANOSTRUCTURES Fundamentals and Applications

www.elsevier.com/locate/photonics

Multi-band left-handed metamaterial inspired by tree-shaped fractal geometry

He-Xiu Xu [a,*], Guang-Ming Wang [a], Chen-Xin Zhang [a], Qiang Liu [a], Zhi-Ming Xu [b], Xin Chen [c], Dai-Liang Zhai [a]

[a] *Missile Institute, Air Force Engineering University, Xi'an 710051, Shaanxi, PR China*
[b] *College of Science, Air Force Engineering University, Xi'an 710051, Shaanxi, PR China*
[c] *National Key Laboratory of Antennas and Microwave Technology, Xidian University, Xi'an 710051, PR China*

Received 27 February 2012; received in revised form 12 May 2012; accepted 27 June 2012
Available online 13 July 2012

Abstract

We report an alternative method of designing a new metamaterial with left handed (LH) characteristics over multi-band (MB) frequencies at microwave frequency regime. The resultant LH metamaterial (LHM) consisting of a single-sided tree-shaped fractal structure features triple magnetic resonances and one electric resonance apart from the lower metal plasma response, which is responsible for the three bands of negative refraction. The multi-resonant mechanism has been systematically studied to account for all electromagnetic behaviors, and capacitor–inductor circuit models are put forward for quantitative analysis. The LHM is balanced in the fundamental passband when only one layer is utilized, whereas the balanced condition is slightly broken when a collection of sub-wavelength cells are cascaded. The negative-zero-positive refraction of the fundamental LH band and the negative refraction of the higher LH band have been numerically validated by a prism-like LHM. For demonstration, a three-layer LHM slab sample is fabricated and measured. Consistent numerical and experimental results are observed. The method not requiring individual resonant particles and electrically continuous wires paves the way for a new route to compact MB LHM design.

Keywords: Left handed metamaterials; Multiband; Negative refraction; Magnetic resonance; Electric resonance

1. Introduction

Left-handed (LH) metamaterials (LHMs) with abundant exotic electromagnetic (EM) properties are termed and envisioned by Veselago decades ago [1] because the electric field (E), magnetic field (H) and wavevector (k) subject to an LH coordinate system. They are made of a periodic collection of subwavelength unit cells and have undergone a burgeoning interest since the first experimental demonstration of negative refractive index (NRI) n [2] inspired by Pendry's encouraging proposal of using split ring resonators (SRRs) [3] and conductor wires [4]. With the explosive development of LHMs in recent years, ample proofs for the existence of NRI with simultaneous negative permeability μ_{eff} and negative permittivity ε_{eff} have been extensively reported in GHz, THz and even visible frequency range [5–21]. Moreover, the potential application of them to build invisibility cloaks [22–24], super lens [25,26] and absorbers [27,28] also become a reality and gain a great impetus. Despite these progressive advancements, most of the LHMs are

* Corresponding author.
E-mail address: hxxu20008@yahoo.cn (H.-X. Xu).

1569-4410/$ – see front matter
http://dx.doi.org/10.1016/j.photonics.2012.06.011

confined to a single frequency operation except for [13–17], which is evidently a considerable drawback and a challenge to practical applications of present LHMs. Furthermore, the acquisition of a negative permeability response over multi-frequency bands is still challenging although the magnetic constituent has been extended from original SRRs and its variations such as Ω-shaped [5] and S-shaped [13] structures to cut-wire pairs [8,18] and fishnet structures [9].

As exposed to fractal geometry, it has been widely adopted by physics and engineering communities due to its two critical natures of space-filling and self-similarity which can be engineered for compact and multifunctional microwave devices and antennas. In spite of this, the application of it to metamaterial is a fresh issue in recent years because sub-wavelength fractal structures exhibit the potential of making metamaterials present interesting resonant properties that are not achievable in conventional metamaterials. A review of literature indicates that only a few LHMs have been available by using this concept [17,29] although many electric resonant [30,31] or magnetic resonant [32,33] single negative metamaterials have been reported. Moreover, most of them were limited to utilizing the H-shaped fractal, making an alternative, improved and simplified fractal LHM that can be easily fabricated and experimentally characterized a pressing task. Most recently, the fractal-perturbed composite right/left handed transmission line (CRLH TL) has been thoroughly studied by the authors [34] to miniaturize the dimensions of cells, making them more appropriate to be described by homogenized effective mediums [35].

In this paper, we propose a completely new multi-band (MB) LHM using tree-shaped fractal to overcome this pressing obstacle. Quite different from previously reported MB LHMs by cascading a chain of subwavelength unit cells or by combining individual electric and magnetic resonators owning scaled geometrical dimensions [13–16], the current multiple magnetic resonances and resultant LH transmission bands are synthesized by using a single-sided integrated planar fractal structure. Multiple magnetic resonances with occurred negative μ_{eff} are introduced by the structure and they can be tuned into the negative ε_{eff} band produced by its plasma and electric resonance response. The paper is organized as follows: in Section 2, the magnetic and electric resonances together with LH bands of one-layer LHM are identified first by material parameters retrieval and then examined by closing gaps of different rings. The balanced condition is also illustrated by the constant equivalence of electric and magnetic plasma frequencies, followed by the mechanisms and controllability of these resonances that are investigated in depth through circuit model analysis, field distribution analysis and lattice constant analysis. In Section 3, both the numerical and experimental results of a multi-layer LHM prism and an LHM slab are provided to confirm the MB negative permittivity, permeability and resultant LH behavior. Section 4 concludes the whole paper.

2. DNG behavior of the balanced one-layer LHM

2.1. LHM cell structure and configuration

Fig. 1 shows the topology and illustrative simulation setup of proposed one-layer (single cell in propagation direction) LHM by etching third-order three-branch tree-shaped fractal metal on one side of a dielectric substrate. The engineered structure built in three iterations is inspired by tree-shaped fractal [36] which

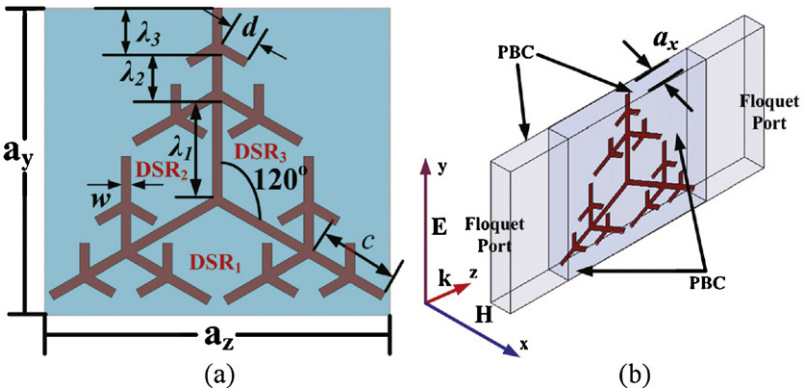

Fig. 1. The illustrative (a) topology and (b) simulation setup of proposed one-cell LHM slab. Detailed geometrical parameters are listed as $c = 1.74$ mm, $d = 0.7$ mm, $w = 0.2$ mm, and $\lambda_1 = 1.969$ mm, $\lambda_2 = 1$ mm, $\lambda_3 = 0.973$ mm.

was initially exploited for a MB antenna design. The construction law of it can be briefly described by the recursive principle as follows: in the first step, three branches originating from one central point with a length of L_1 and an angle of 120° interval are engineered for the initiator, followed by considering three ends of these branches as fresh starting points. Each of them produces three new branches with a length of L_2 and an angle of 120° interval. Taking this repeated procedure in a recursive fashion, the third and higher-order self-similar tree-like fractals are formed as a function of iteration factor F and iteration order n:

$$L_n = \frac{L_1}{F^{(n-1)}} \tag{1}$$

Note that L_3 is selected larger than L_2/F in this particular design to guarantee the small gap space which can be adjusted to tailor the magnetic resonant frequency and accordingly facilitates a balanced condition. An inspection of the configuration implies that many diamond split rings (DSRs) are formed by different levels of ternary branches with different sizes. Consequently, a set of magnetic resonances are expected because circular currents are excited in these scaled DSRs when response to the normal-to-plane magnetic field, in analogy to conventional SRRs [2,3]. To the best of our knowledge, the proposed tree-shaped LHM draws some similarity to the dendritic LHM but essentially different from it [11] in producing negative magnetic response over multiple frequencies. The structure has ternary rotational symmetry along three directions and thereby exhibits an identical electric response when the polarization rotates 120°. Therefore, even uniform sized DSRs at different positions may response with different magnetic resonate frequencies. Only when a correctional factor a_i is introduced, can the frequency-dependent μ_{eff} at ith magnetic resonance $\omega_{m0}^{(i)}$ obey Lorentz-type dispersion [3]:

$$\mu_{eff}(\omega) = 1 - a_i \frac{\omega_{mp}^{(i)^2} - \omega_{m0}^{(i)^2}}{\omega^2 - \omega_{m0}^{(i)^2} + i\gamma\omega} \tag{2}$$

$$\omega_{mp}^{(i)^2} = \frac{\omega_{m0}^{(i)^2}}{1 - F_i} \tag{3}$$

where $\omega_{mp}^{(i)}$ is the ith magnetic plasma frequency, γ is the damping factor and F_i (smaller than unity) is the filling factor of the ith resonator, namely the ratio of area of the interior ring to that of total resonator.

As to the electric response, the fundamental negative ε_{eff} band is available below the fundamental plasma frequency $\omega_{ep}^{(0)}$ (Drude-type dispersion) originating from the oscillation of linear current of the vertical branch. The mechanism of the resultant plasma is similar to that of a thin wire. Despite this, a higher electric resonance $\omega_{e0}^{(1)}$ is envisioned below the second plasma frequency $\omega_{ep}^{(1)}$, and the resultant ε_{eff} takes the Lorentz law:

$$\varepsilon_{eff}(\omega) = 1 - \frac{\omega_{ep}^{(1)^2} - \omega_{e0}^{(1)^2}}{\omega^2 - \omega_{e0}^{(1)^2} + i\gamma\omega} \tag{4}$$

Note that $\omega_{e0}^{(1)}$ is introduced by the discontinuity of the gap in DSR_2 or namely the oscillation of linear current through the gap capacitor, which will be validated in the upcoming section.

To validate the speculation and characterize the unique feature of the proposed tree-shaped LHM slab, numerical simulations are performed for one-layer structure by using commercial finite element-based EM field solver Ansoft's High Frequency Structure Simulator (HFSS). In the simulation setup shown in Fig. 1(b), the metal patterns with zero-thickness height are assigned as perfect electrical conductor (PEC) which is a tradeoff between accuracy and computer resources. They are placed in the center of a substrate to avoid any intersecting boundary condition in software. This disposal does not affect the rationality of calculated results owing to the LHM periodicity. Note that the metal we used in the fabricated prototype is copper with conductivity of $\sigma = 5.8 \times 10^7$ S/m and thickness of $t = 0.036$ mm. The unit cell is put into a cubic chamber of $a_x \times a_y \times a_z = 1$ mm $\times$ 6.4 mm $\times$ 7.2 mm. The transverse EM (TEM) wave was incident along z-direction with the electric field polarized parallel to y-axis and magnetic field along x-axis. Four boundaries along x- and y-directions are assigned as periodic boundary conditions (PBC) (master/slave in the Ansoft HFSS) to mimic infinite arrays in xoy plane perpendicular to the propagation direction. This setup is a good approximation to the measurement environment in the waveguide which operates in its dominant TE10 mode. The substrate which the tree-shaped metal is deposited on is FR4 substrate with a dielectric constant $\varepsilon_r = 4.3$, thickness $h = 1$ mm and loss tangent $\tan\delta = 0.02$. Although the FR4 is rather lossy at microwave frequencies, it is widely available and is appropriate for this implementation.

2.2. Identification of magnetic and electric resonances, and balanced condition

Here we follow a similar method proposed in [35] to check the resonances of DSRs, whereas the method is

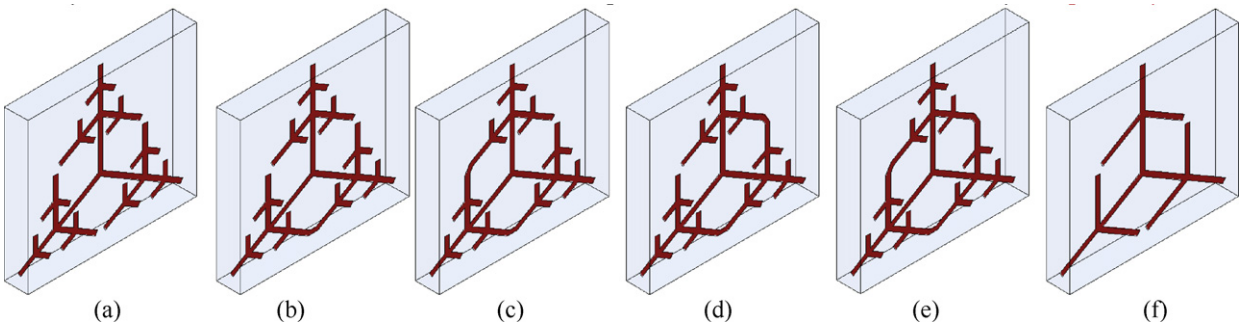

Fig. 2. Schematics of the proposed tree-like LHM slabs under different cases. (a) Third-order tree-shaped LHM slabs with three open gaps (case 1), (b) closed bottom gap (case 2), (c) open right gap (case 3), (d) open left gap (case 4) and (e) three closed gaps (case 5); (f) second-order LHM slab with three open gaps (case 6).

applied to check the resonance of Ω-shaped ring in previous work. To this end, we carry out extensive simulations on proposed LHM slabs in different cases, namely LHMs constructed with different DSRs (DSR_1, DSR_2 and DSR_3) formed through the first and second levels of ternary branches. The closed gaps are realized by connecting the ends of two adjacent sections. In this way the driven force of circulating currents will be eliminated. Totally, five conditions regarding different gaps are considered from cases 1 to 5. Fig. 2 shows the schematics of these one-layer LHM slabs. Note that the second-order tree-shaped LHM slab (case 6) shown in Fig. 2(f), is also analyzed to identify the influence of DSRs formed through the second and third levels of ternary branches on the LH performance. Using aforementioned simulation setup, the complex transmission and reflection characteristics are illustrated by the full-wave S-parameters.

To provide a physical insight and identify the left-handedness or right-handedness, the standard inverted algorithm [38,39] is applied to retrieve effective constitutive material parameters from S-parameters. It is worth mentioning that the material parameters in cases 3 and 4 are retrieved using the method developed in [40] which was tailored for bianisotropic metamaterials. This is because the magnetoelectric coupling is induced in these cases because of the asymmetry of the structure in z-direction. Similar to SRRs, the electric field in the y-direction can induce a magnetic dipole in the x-direction due to the asymmetry of gaps, whereas the magnetic field in the x-direction also introduces an electric dipole in the y-direction. The ambiguity of real parts of the refractive index $\mathrm{Re}(n)$ and impedance $\mathrm{Re}(z)$ has been cautiously addressed with obedience to the robust retrieval procedure [38] as well as the causality and passivity.

Fig. 3 compares the simulated S-parameters and retrieved constitutive material parameters of the proposed one-cell LHM slabs between cases 1 and 6 in a broad frequency range. Referring to Fig. 3(a), two passbands are evidenced from two obvious transmission peaks in both cases. A reflection valley of −18.1 dB at 8.44 GHz for the lower fundamental peak and a valley of −5.52 dB at 14.8 GHz for the upper second peak are ambiguously shown in case 1, whereas these reflection valleys are observed to be −29.4 and −5.62 dB at 8.79 and 15.4 GHz, respectively in case 6. The reflection coefficients imply that both LHMs are well matched to the free space in the fundamental band, whereas the impedance matching performances deteriorate to some degree in the upper band. The higher-order fractal perturbation induces a substantial red shift of frequencies on the order of 4% due to the increased dimensions of branches in a fixed footprint while it does not affect significantly the impedance match, illustrating a possibility of making compact metamaterial devices by utilizing high-level fractal structures.

Consulting Fig. 3(b) and (c), the material parameters suffer accordingly a red shift in higher-order fractal implementation, accounting for the red shift of S-parameters. Moreover, three magnetic resonances $\omega_{m0}^{(1)}, \omega_{m0}^{(2)}, \omega_{m0}^{(3)}$ and one electric resonance $\omega_{e0}^{(1)}$ exhibit in both cases, implying that they are induced by DSR_1, DSR_2 and DSR_3 rather than DSRs formed through the second and third levels of ternary branches. The magnetic plasma frequencies obtained by insertion of $\omega_{m0}^{(1)}, \omega_{m0}^{(2)}$, and $\omega_{m0}^{(3)}$ into Eq. (3) are in reasonable agreement with those simulated ones which are identified as the cross-zero point of the real part of permeability $\mathrm{Re}(\mu_{eff})$ or the cutoff frequency of negative $\mathrm{Re}(\mu_{eff})$. In case 1, $\mathrm{Re}(\mu_{eff})$ takes negative values in the frequency scope of 7.63–8.41, 8.94–11.63, and 14.18–16.54 GHz, whereas the real part of permittivity $\mathrm{Re}(\varepsilon_{eff})$ undergoes negative below 8.41 GHz and in 10.54–15.03 GHz. Therefore, three LH bands with simultaneous negative $\mathrm{Re}(\mu_{eff})$ and

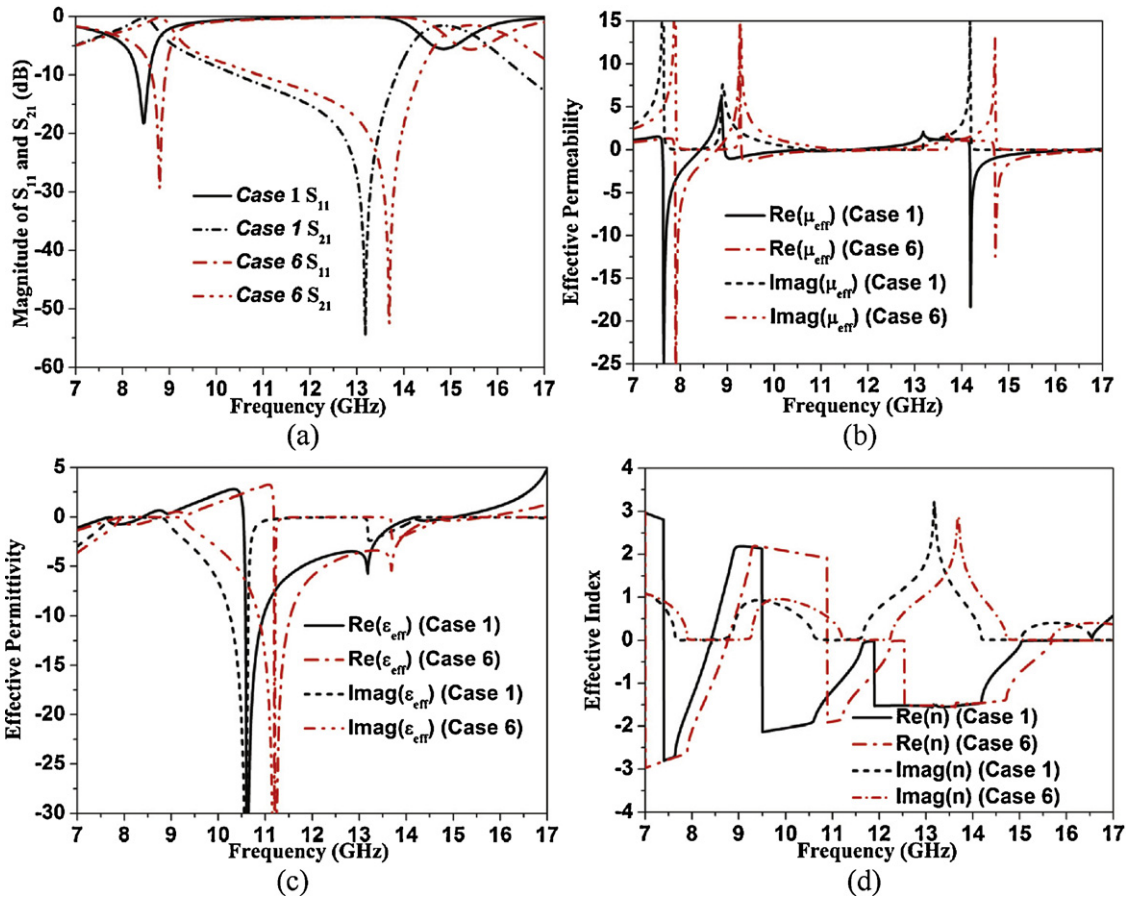

Fig. 3. Comparison of simulated S parameters as well as effective material parameters between cases 1 and 6. (a) Magnitudes of S_{11} and S_{21}; (b) effective Re(μ_{eff}); (c) effective Re(ε_{eff}) and (d) effective Re(n).

Re(ε_{eff}) are 7.63–8.41, 10.54–11.63, and 14.18–15.03 GHz which coincide well with three regions of negative Re(n) depicted in Fig. 3(d). Remark that the negative permittivity is strongly dispersive in the vicinity of electric resonance. In both cases, the fundamental composite passband consisting of not only a lower LH contribution (supporting a backward wave) but also a higher right handed (RH) band (8.41–8.94 GHz, supporting a forward wave) is balanced without any forbidden interval [6]. The balanced condition which is a most exciting characteristic is achieved from an equality of the magnetic and electric plasma frequencies $\omega_{mp}^{(1)} = \omega_{ep}^{(0)}$. The $\omega_{ep}^{(0)}$ can be formulated in a first approximation by Pendry's formula [4]:

$$\omega_{ep}^{(0)} = \frac{2\pi c_0^2}{a^2 \ln(a/r)} \tag{5}$$

where a and r are the periodicity of wire array and wire radius, respectively. Note that the case we dealt with is the rectangle cuboid rather than circular rod in [4]. Nevertheless, the plasma frequency takes the same function as the current metal patterns can be transformed to equivalent rods with corresponding r as a function of w.

The bandwidth of negative Re(n) is wider than that of overlapped negative Re(μ_{eff}) and Re(ε_{eff}). This phenomenon, seemingly unphysical, is induced by the periodic effects of the retrieval procedure [8]. The reason is that we can achieve Re(n) negative provided that $\mathrm{Im}(\varepsilon_{eff})\mathrm{Im}(Z) > \mathrm{Re}(\varepsilon_{eff})\mathrm{Re}(Z)$, where $Z = \sqrt{\mu_{eff}/\varepsilon_{eff}}$ is the effective impedance. Therefore, Re(n) in the frequency region of single negative Re(μ_{eff}) or Re(ε_{eff}) is typically accompanied with a large Im(n) associated with losses. The losses measured by the figure of merit (FOM) = $-$Re(n)/Im(n) [7] in these single negative regions are obtained smaller than those in double negative regions, giving strong support to this declaration. It is worth mentioning that there are also higher magnetic resonances occurring at 20.9 and 22.3 GHz, respectively corresponding to the resonance of DSRs formed by the second and third levels of

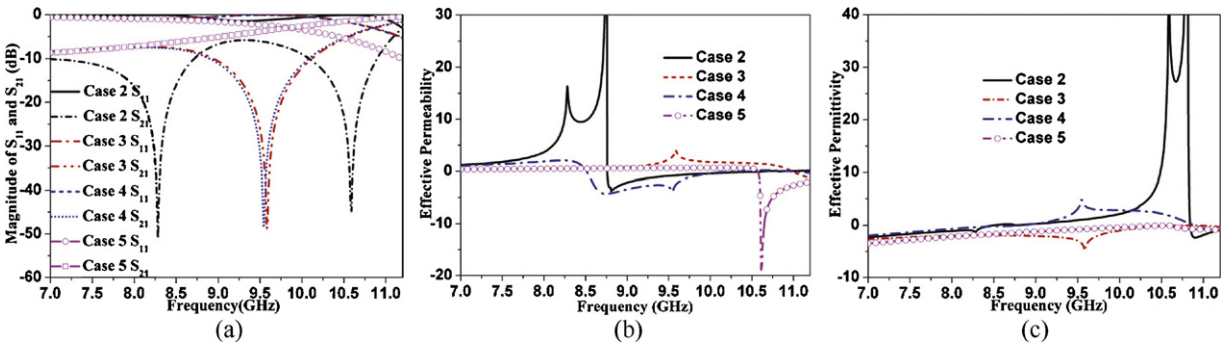

Fig. 4. Comparison of simulated S parameters as well as effective constitutive material parameters among cases 2–5. (a) Magnitudes of S_{11} and S_{21}; (b) effective Re(μ_{eff}); and (c) effective Re(ε_{eff}).

ternary branches. However, it reversely does not show any evidence of this phenomenon for the second-order LHM, implying that the variously emerged current loops are the key factors of the MB negative magnetic response. The higher magnetic resonances are excluded from our discussion because they are out of scope in terms of a LH behavior and an effective medium [35] where dimensions of a cell are restricted to small fractions of a wavelength at operating frequency.

To illustrate the physical mechanism of the multiple resonances of the proposed tree-shaped LHM, Fig. 4 compares the simulated S-parameters and the retrieved effective material parameters of the one-cell LHM slabs in a narrow frequency range among cases 2–5 (closed DSR_1). As can be observed, the aforementioned composite passband are replaced by a wide stopband with various dips in the transmission spectrum, resulting from a single negative permittivity. The absence of the fundamental magnetic resonance in these four cases implies that DSR_1 accounts for $\omega_{m0}^{(1)}$, whereas the almost fixed $\omega_{m0}^{(2)}$ in cases 1, 2 and 4 (open DSR_2) and the absence of $\omega_{m0}^{(2)}$ in closed DSR_2 in cases 3 and 5 indicate that DSR_2 is responsible for $\omega_{m0}^{(2)}$. The absence of $\omega_{m0}^{(3)}$ from case 2 to case 5 illustrates that the gaps in three DSRs are necessary for $\omega_{m0}^{(3)}$. Referring to Fig. 4(c), the cross-zero point of negative permittivity ($\omega_{ep}^{(0)}$) is observed as 8.41, 8.5 and 8.84 GHz whereas $\omega_{e0}^{(1)}$ occurs at 10.54, 10.85 and 10.9 GHz in cases 1, 2 and 4, respectively. However, it reversely dose not show any electric resonances in cases 3 and 5. Moreover, $\omega_{ep}^{(0)}$ in these two cases is obtained as 14.6 and 14.1 GHz, respectively, showing evidently a sharp blue shift in comparison to $\omega_{ep}^{(0)}$ in the open DSR_2. Thereby we conclude that $\omega_{ep}^{(0)}$ and $\omega_{e0}^{(1)}$ are significantly affected by the gap in DSR_2 and in contrast have nothing to do with the gaps in DSR_1 and DSR_3.

2.3. Surface currents and fields distribution, and circuit model analysis

To further validate the underlying multi-resonant mechanism from a physical insight, we begin with the analysis from a perspective of currents and fields distribution and followed by a circuit model analysis in this section. For currents and fields calculation, the tree-shaped metal is moved to the surface of a substrate. Fig. 5 depicts the surface currents distribution of the proposed LHM. As can be seen in Fig. 5(a), DSR_1 resonates at 7.65 GHz in response to external magnetic field and the localized clockwise surface current loop (see the blue arrow) with strong density is fashioned, accounting for the strong fundamental magnetic

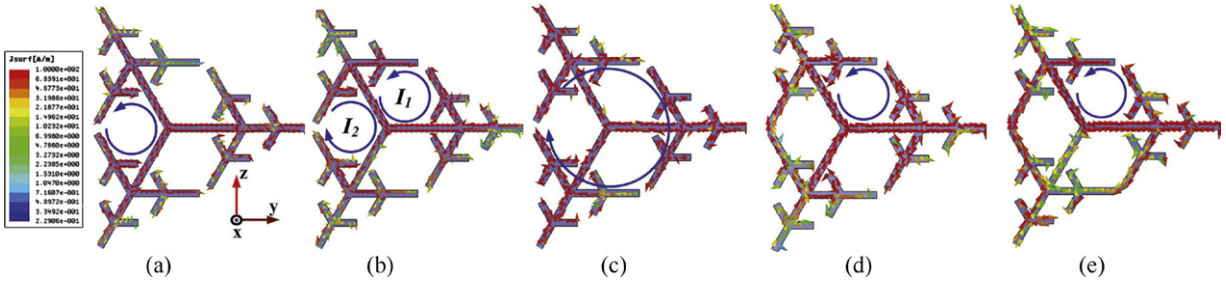

Fig. 5. Currents distribution on metallic patterns at three magnetic resonances in case 1 (a) 7.65 GHz, (b) 8.95 GHz and (c) 14.2 GHz in conjunction with currents distribution at (d) 8.8 GHz in case 2 and (e) 8.55 GHz in case 4.

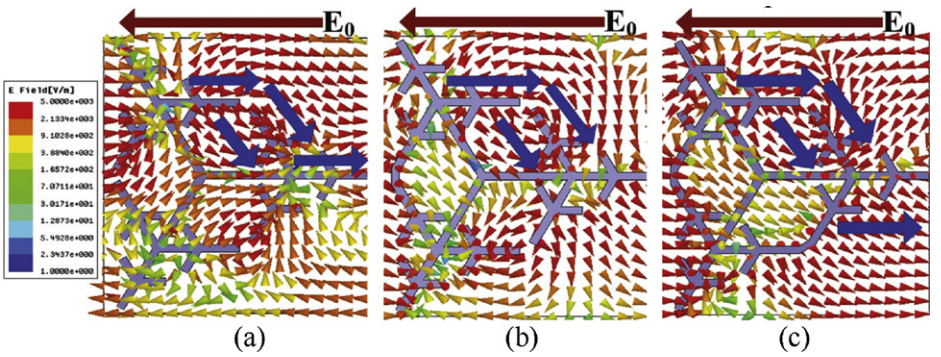

Fig. 6. Electric field distribution in substrate board at electric resonance. (a) 10.6 GHz in case 1, (b) 10.9 GHz in case 2 and 10.95 GHz in case 4.

resonance. Note that the resonance of DSR_1 also yields a weaker surface current loop in DSR_2 due to the interaction. From Fig. 5(b), the origin of $\omega_{m0}^{(2)}$ associated with DSR_2 is corroborated according to the enhanced clockwise current loop concentrated in this region. This declaration finds strong support from the current distribution shown in Fig. 5(d) and is further validated by that shown in Fig. 5(e). The DSR_2 resonates with almost constant frequency no matter whether the gaps in DSR_1 and DSR_3 are open or not. In like manner, the resonance of DSR_2 is also accompanied with a parasitical surface current loop in DSR_1. Distinguished from Fig. 5(a), the parasitical current strength is several orders larger than that of Fig. 5(a), thus the mutual effect of DSR_1 is not negligible. Consulting Fig. 5(c), the shaped biggest current loop formed in the conjunct area of DSR_1, DSR_2 and DSR_3 through three cascaded gaps is responsible for the $\omega_{m0}^{(3)}$. Among these cases, current loops behave to resemble several independent magnetic dipoles whose dipole moments drill through these loops and are anti-parallel to the external magnetic field. This is especially true in case 1 which fashions tri-band negative μ_{eff} in the vicinity of three magnetic resonances.

The electric field distributing in the substrate board of proposed LHM is plotted at electric resonance in Fig. 6. The charges with reverse polarity are accumulated at both ends of the gap in DSR_2 in cases 1, 2 and 4, resembling an electric dipole. The inductive net electric dipole moments yield when current flows on the tree-shaped metal patterns and are anti-parallel to the incident electric fields E_0, providing the negative permittivity. Note that the field calculation is also performed for cases 3 and 5 and these results are not given for brevity of content. Although DSR_3 also owns a gap and is capable of providing a capacitance, it is unable to excite the oscillation of current and play the role of accumulating charges whose dipole moments are anti-parallel to E_0. The uniform inductive electric field with respect to E_0 and the absence of electric resonance in case 3 (open DSR_3) give strong support to this interpretation.

On the basis of the aforementioned simulation results, we establish an equivalent circuit model (see Fig. 7) for the proposed tree-shaped LHM cell regarding three magnetic resonances and one electric resonance. This can be carried out because the dimension of LHM cell is a small fraction of the free-space wavelength evaluated at operating frequency. The circuit shown in Fig. 7(a) models the fundamental magnetic resonance, where L_0 represents the inductance of section λ_1, C_0 models gap capacitance and R is the resistance accounting for losses. Note that L_0 is composed of both self-inductance and mutual inductance between adjacent cells arranged in x direction. According to the current loop shown in Fig. 5(a), the total inductance comprises four parts, namely the inductance of two λ_1 and inductance of two $\lambda_2 + \lambda_3$. Since $(\lambda_2 + \lambda_3)/\lambda_1 \approx 1$, the total inductance of loop DSR_1 is roughly calculated as $4\alpha L_0$, where $\alpha \leq 1$ is

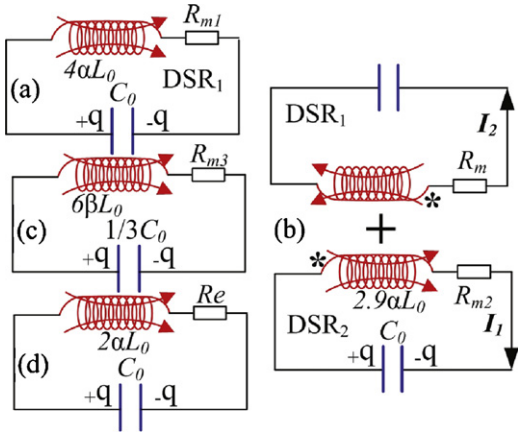

Fig. 7. Equivalent circuit model of the proposed LHM at (a) $\omega_{m0}^{(1)}$, (b) $\omega_{m0}^{(2)}$, (c) $\omega_{m0}^{(3)}$, and (d) $\omega_{e0}^{(1)}$.

the correctional factor by taking the effect of non-alignment configuration into account. Given the lumped elements, the $\omega_{m0}^{(1)}$ is directly formulated as:

$$\omega_{m0}^{(1)} = \frac{1}{2\sqrt{\alpha L_0 C_0}} \tag{6}$$

As to $\omega_{m0}^{(2)}$, the mutual effect of DSR_1 is significant as discussed above. Denote the currents flowing along DSR_1 and DSR_2 I_2 and I_1, respectively. Since the currents are superposed in the conjugate section of these two DSRs, the equivalent inductance of this section that contributes to DSR_2 is calculated as:

$$L_{01} = \frac{I_1}{I_2 + I_1} L_0 \tag{7}$$

As I_1 is larger than I_2, the total inductance of DSR_2 is roughly evaluated as $2.9\alpha L_0$ by taking $I_1/I_2 = 2.64$ which is calculated from current density. Consequently, we derive $\omega_{m0}^{(2)}$ as $\sqrt{4/2.9}\omega_{m0}^{(1)}$. Take $\omega_{m0}^{(1)}$ as 7.65 GHz, $\omega_{m0}^{(2)}$ is achieved as 8.98 GHz which is quantitatively very similar to 8.95 GHz obtained from the full-wave simulation.

As to $\omega_{m0}^{(3)}$, the loop inductance is assessed as $6\beta \times L_0 = 6\beta L_0$ ($\beta \le \alpha \le 1$) and the capacitance is $1/(1/C_0 + 1/C_0 + 1/C_0) = C_0/3$, where β is also a correctional factor by taking the quasi-circular configuration into account. Taking $\alpha/\beta = 1.7$, then $\omega_{m0}^{(3)} = \sqrt{2\alpha/\beta}\omega_{m0}^{(1)}$ is roughly achieved as $1.84\omega_{m0}^{(1)}$, which coincides reasonably with $1.85\omega_{m0}^{(1)}$ obtained from the full-wave simulation. The discrepancy is put forward by the inductances and capacitances of DSRs formed through the third level of branches and gaps. When it comes to the electric resonance, at least two wire sections and a gap are involved in the production of an electric dipole according to Fig. 6. The inductance is $L_e = 2\alpha \times L_0 = 2\alpha L_0$ while the capacitance is $C_e = C_0$, hence $\omega_{e0}^{(1)}$ is engineered as $\omega_{e0}^{(1)} = \sqrt{2}\omega_{m0}^{(1)}$ which is consistent with $1.38\omega_{m0}^{(1)}$ achieved from the full-wave simulation. To sum up, the equivalent circuit model describes qualitatively all magnetic or electric resonances. The variation of any geometrical parameters corresponding to the change of inductances and capacitances in the circuit would cause the shift of resonant frequencies. This analysis provides us a quantitative prediction of residual resonant frequencies whenever a magnetic or electric resonant frequency is given and in turn affords a good guideline for individual control over these resonances.

2.4. Lattice constant analysis

Although the applicability of the standard procedure has been significantly extended to a metamaterial whose cell dimensions are comparable to the free-space wavelength [41], the material parameters hardly describe the macroscopical EM behavior. To ascribe μ_{eff} and ε_{eff} to the LHM appropriately, we will concentrate our attention on the investigation of the former two magnetic resonances and the corresponding two LH bands. Two complementary parameters analysis are carried out to illustrate physically the dependence of magnetic/electric resonances as well as the resulting LH behavior upon the lattice constants a_x and a_y. Fig. 8 presents the influence of a_x. The residual geometrical parameters are maintained the same as those shown in Fig. 1. As Fig. 8(a) illustrates, the transmission peak of the fundamental LH band undergoes a mild blue shift from 8.45 to 9 GHz as a_x arises from 1 to 2 mm step by 0.5 mm. Referring to Fig. 8(b) and (c), the magnetic resonant frequencies and electric plasma frequency shift upwards as a_x increases. The blue shift takes a mild variation as a_x, e.g., $\omega_{m0}^{(1)}$ increases form 7.65 to 8.45 and finally to 8.75 GHz whereas $\omega_{mp}^{(1)}$ shifts upwards from 8.41, 8.96 to 9.09 GHz and $\omega_{ep}^{(0)}$ changes orderly from 8.41, 8.88 to 9.01 GHz. The almost identical blue shift of $\omega_{m0}^{(1)}$, $\omega_{mp}^{(1)}$ and $\omega_{ep}^{(0)}$ is a key factor of the variational composite passband. Moreover,

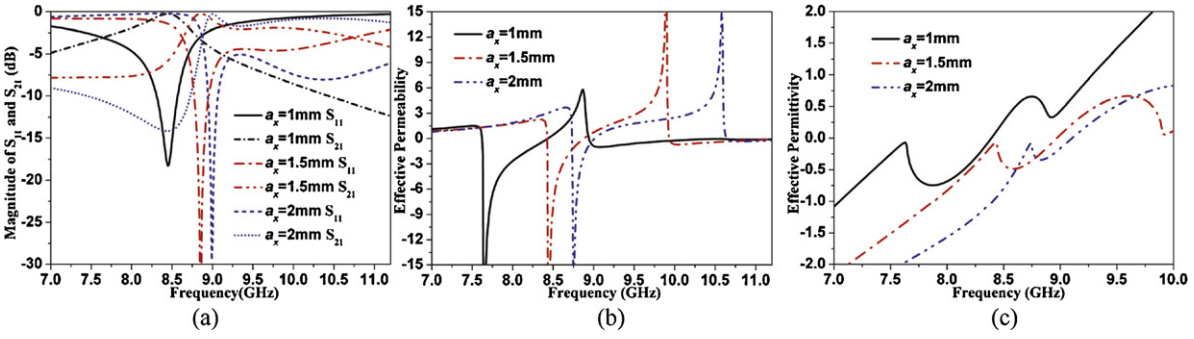

Fig. 8. The dependence of simulated S-parameters and effective material parameters as functions of a_x. (a) Magnitudes of S_{11} and S_{21}, (b) effective $\mathrm{Re}(\mu_{eff})$; and (c) effective $\mathrm{Re}(\varepsilon_{eff})$.

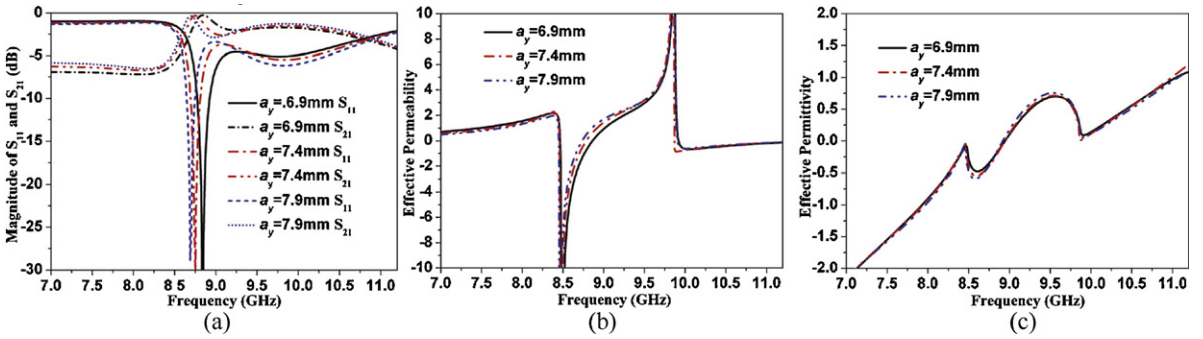

Fig. 9. The dependence of simulated S-parameters and effective material parameters as functions of a_y. (a) Magnitudes of S_{11} and S_{21}; (b) effective Re(μ_{eff}); and (c) effective Re(ε_{eff}).

the decrease of a_x induces a broader band of negative permeability and in turn a broader fundamental LH band due to an enhanced normal-to-plane coupling. This physical phenomenon coincides well with that was drawn in [37] where the decreased periodicity between Ω patterns increased the bandwidth of resonance band gap (negative μ_{eff}). Although the increase of a_x does not face a significant amount of reflection, it slightly breaks down the strict balanced condition in a continuous negative-zero-positive index dispersion. Nevertheless, the disturbed band is so narrow that it can be negligible in a wide frequency range. Therefore, the LHM slabs with large a_x are still balanced related to a relaxed balanced condition. Not to lose generality, we also perform extensive simulations on LHMs with larger a_x. An exciting characteristic is that these LHMs are always balanced with a quasi equality of $\omega_{mp}^{(1)}$ and $\omega_{ep}^{(0)}$.

Given the quite sensitivity of the magnetic resonances to a_x, it is advisable to choose the periodicity as the height of a substrate to eliminate any tolerances in the fabrication of an LHM. The variation of $\omega_{ep}^{(0)}$ is evident according to Eq. (5) in virtue of changed a. The fluctuation of $\omega_{m0}^{(1)}$ can be elucidated by considering a column of DSR loops along x direction as a quasisolenoid due to the periodicity of LHM. A column of DSR loops behave indeed like a solenoid. Here we assume that the fringing effect generated when currents flow around the solenoid is negligible [42]. Therefore the inductance of each ring of the solenoid composed of infinite DSRs is calculated as:

$$L = \frac{\mu_0 S_{DSR}}{a_x}(H). \tag{8}$$

where S_{DSR} is the area of DSR loop. According to Eqs. (6) and (8), $\omega_{m0}^{(1)}$ increases accordingly as a_x.

The effect of a_y on magnetic and electric resonances is illustrated in Fig. 9. Note that a_x maintains as 1.5 mm and the residual geometrical parameters are fixed as Fig. 1. As Fig. 9 illustrates, almost constant S-parameters, Re(μ_{eff}) and Re(ε_{eff}) are observed as a_y increases from 6.9 to 7.9 mm step by 0.5 mm. The slight red shift of $\omega_{m0}^{(1)}$ is the cause of the shifted composite passband. Moreover, the relaxed balanced condition is always satisfied with negligible discontinuity in negative–zero–positive index dispersion. We conclude that the interplay between adjacent cells along y-direction is weak and can be negligible. Therefore, the distance between top-and-bottom cells should be tuned infinitely small from the effective medium angle.

3. DNG behavior of the MB multi-layer LHM

To validate the DNG behavior and multi-resonant behavior of LHM composed of multi cells in propagation direction, two complementary simulations are performed individually. The former one is the multi-layer LHM slab while the latter one is the multi-layer LHM prism.

3.1. Numerical and experimental results of multi-layer LHM slabs

Fig. 10 shows the simulation setup and schematic illustration of proposed multi-layer LHM slab. The setup shown in Fig. 10(a) is the same as that of one-cell LHM slab. For experimental demonstration, a bulk LHM slab example whose schematic and prototype are shown in Fig. 10(b) and (c) is designed, fabricated and measured. In fabrication, 28 substrates on which tree-shaped metal patterns are positioned are tightly stacked alternatively, then put together by adhesives and finally reinforced by a hot press. The substrate parameters are

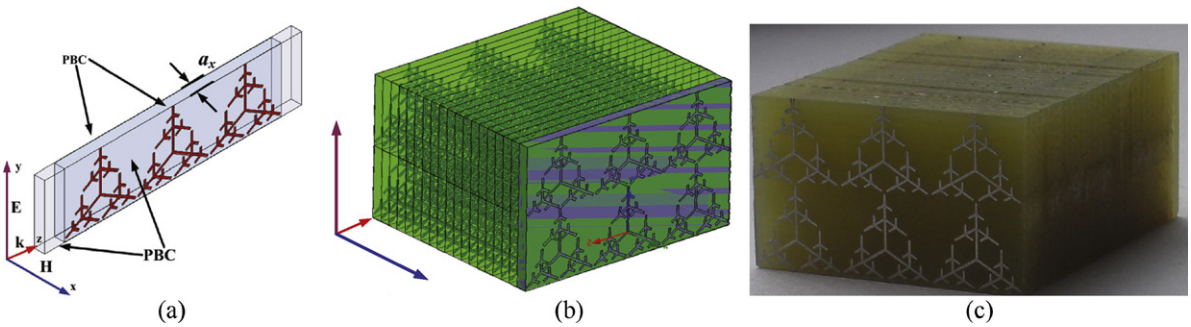

Fig. 10. (a) Simulation setup, (b) schematic and (c) photograph of designed LHM composed of three layers in propagation direction.

kept the same as those in simulation and the unit cell is extended to $28 \times 2 \times 3$ of the original LHM elements illustrated in Fig. 1. In measurement, the sample was put into a standard waveguide BJ84. The transmission and reflection spectra of the fabricated LHM are recorded by an Agilent network analyzer HP8720ES.

To illustrate the influence of number of cells along propagation direction, three slab-shaped LHMs regarding one, two and three layers are characterized, respectively for numerical study. Fig. 11 compares the transmission and reflection spectra in conjunction with the retrieved material parameters. Note that LHM slabs with four and five cells along propagation are also analyzed and the results are not given for clarity of Fig. 11. Consulting Fig. 11(a), the wider transmission band perturbed by several reflection tips indicates large

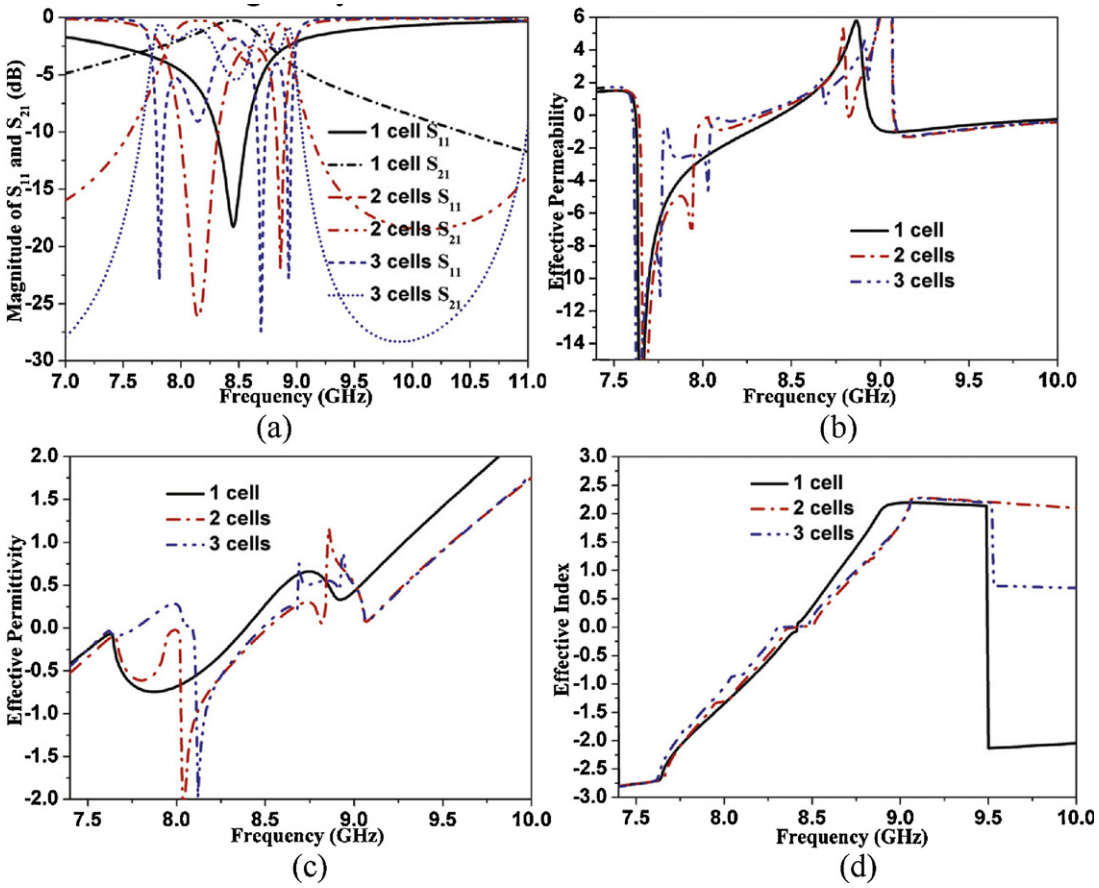

Fig. 11. Comparison of simulated S-parameters as well as effective material parameters between LHMs owning one, two and three layers along propagation direction (a) magnitudes of S_{11} and S_{21}; (b) effective Re(μ_{eff}); (c) effective Re(ε_{eff}) and (d) effective Re(n).

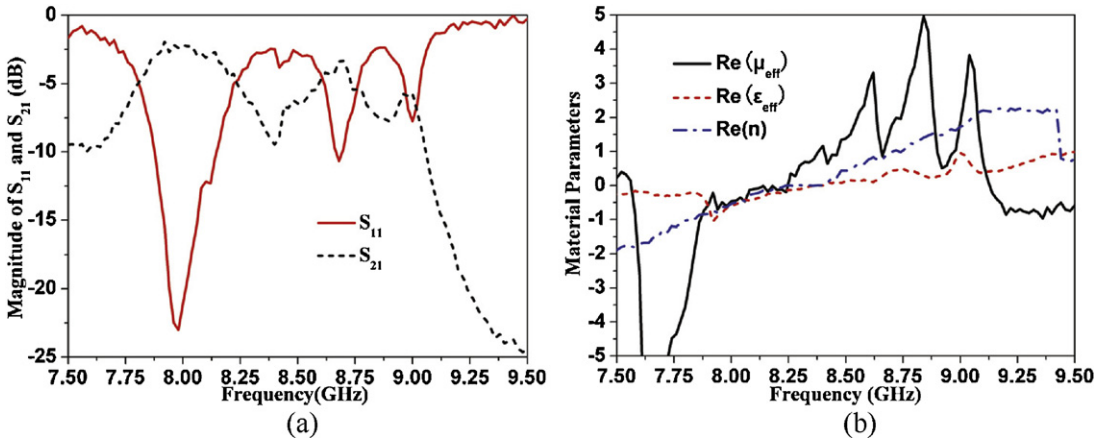

Fig. 12. The measured S-parameters and retrieved material parameters. (a) Magnitudes of S_{11} and S_{21}; (b) effective Re(μ_{eff}), Re(ε_{eff}) and Re(n).

oscillations, illustrating the significance of the coupling effects generated between adjacent cells in propagation direction. This is especially true when a new weak current loop is shaped in four adjacent cells in the top-and-down and left-and-right regime of a tree-shaped LHM. In addition to the coupling, the truncation of the structure also results in the large ripples [6]. The exhibited shallow dips in-between transmission passband imply that the LHMs with multi layers are not balanced anymore. A further inspection of this figure also indicates that the out-of-band suppression level at the lower and upper edge of the passband induced by a single negative permittivity or a negative permeability enhances with the number of unit cells. The wider and deeper suppression gap resembles the resonance gap of periodically arranged Ω-shaped patterns through the normal-to-plane coupling which is well established in [37].

Accordingly, the retrieved material parameters of LHMs owning one single cell are different from those of LHMs containing a chain of unit cells as is shown in Fig. 11(b)–(d), which coincides well with the conclusions drawn by Koschny et al. [43] and Zhou et al. [44] from LHMs composed of SRRs/wires and fishnet structures, respectively. This is especially true for the much discrepancy introduced in $\omega_{m0}^{(2)}$ between one-layer and multi-layer LHMs although almost identical $\omega_{m0}^{(1)}$ is observed. As expected, a small forbidden band interrupts in the transition from the LH band to RH band in the case of multi-layer LHM. This is because the cell size is on the order of λ/6 which is far from approaching the criterion of λ/30 validated in Koschny's study [43]. Notice that the S-parameters and retrieved material parameters converge to common values as the number of the cells increases, which can be clearly evidenced from the almost identical results of LHMs owning four, five and even more cells along propagation. The convergent length dependence is a required property to attribute effective medium behavior to a metamaterial and the converged results are different from those of LHM having only one unit cell. Nevertheless, a generally satisfying agreement among these cases ambiguously illustrates the homogeneity of the LHM and also correctness of the retrieval procedure.

Fig. 12 illustrates the measured frequency spectrum in conjunction with retrieved material parameters of the fabricated LHM slab in a narrow frequency range. The frequency responses at higher frequencies are not given due to the cut-off frequency of the waveguide BJ84. Nevertheless, the LH characteristic at these frequencies will be corroborated by a complementary analysis of a prism in the upcoming section. Very reasonable agreement between simulation and measurement is observed except for slightly wider LH and RH bands together with slightly larger insertion losses in the measurement case. This deviation mainly originates from the losses in FR4 substrates and partially from the adhesives that are used for robustness in the experiment whose dielectric tangent loss is larger than that of the practically used substrate. The lossy effect enhances as frequency increases. Nevertheless, three transmission peaks with considerable intensity on the order of −2.2, −3.3 and −5.6 dB are clearly observed at 7.98, 8.68 and 9 GHz, respectively. Following Fig. 12(b), one can learn that Re(μ_{eff}) takes negative values in 7.58–8.26 and 9.12–9.5 GHz, respectively, whereas the Re(ε_{eff}) undergoes negative in 7.5–8.39 GHz. Therefore the LH band (overlapped negative ε_{eff} and negative μ_{eff}) covering the fundamental transmission peak is ranged from 7.58 to 8.26 GHz, whereas the RH band comprising the residual two transmission peaks occurs in 8.39–9.12 GHz. In between, a narrow unbalanced stopband

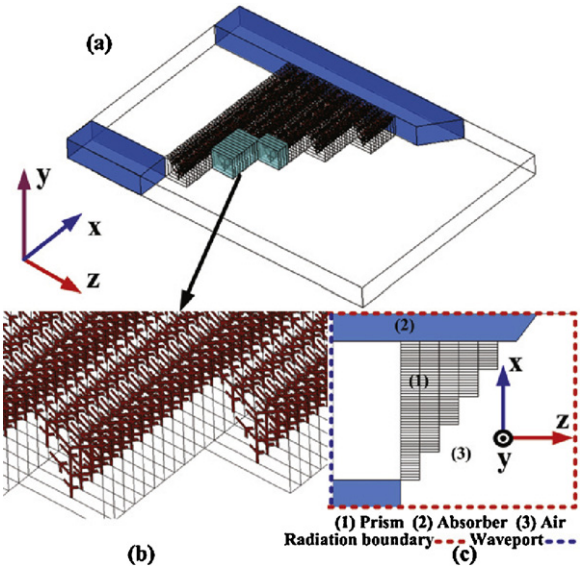

Fig. 13. Illustration of the simulation of negative refractive fraction. (a) 3D view of prism-shaped LHM sample; (b) megascopic view of the stairs; (c) top/bottom view of the simulation setup.

(single negative ε_{eff}) is validated from 8.26 to 8.39 GHz. Again, the ripples in transmission spectrum are comparable with respect to those exhibited in simulations.

3.2. DNG behavior of an LHM prism

Prism-shaped structures have been demonstrated as a good strategy to find the sign and value of a refractive index [2,6]. Here we construct and study numerically a prism-shaped LHM with a prism angle of $\theta_i = \arctan(a_z/10a_x) \approx 35.7^\circ$ as illustrated in Fig. 13. Although a larger prism sample would be beneficial for an accurate refractive index which would be useful for a quantitative analysis, the complex structure consumes a mass of computer resources and time. The wedge prism composed of five stairs is a good tradeoff between accuracy and computer resources on a local server and is sufficient for a qualitative analysis, one-unit-cell spacing along z-direction (propagation direction) and ten-unit-cell step along x-axis. One cell is considered in y-direction because the coupling along this direction is weak and is not necessary to construct the LH behavior. Therefore, a chain of maximum 50 unit cells along x-direction are positioned between two top-and-bottom parallel plates with PEC boundary, whereas 1 and 5 unit cells are utilized at the first and the last stairs, respectively along z-direction. As is evident from the simulation setup shown in Fig. 13(c), the transverse EM wave is normally incident (wave-port excitation) and the power intensity is tailored by a side absorber. The front-and-back surfaces as well as the right ones are assigned as radiation boundary to detect the refraction pattern. The incident angle is denoted as θ_i, whereas the refracted angle θ_r is characterized as the scan angel of a beam peak in a far field radiation pattern relative to the plane normal to the tilted interface.

Fig. 14 gives the maps of electric-field magnitude at five different frequencies in the midplane ($y = 3.2$ mm). As is shown, the magnitudes of refracted beams are enhanced as frequency increases, making the intensity at 8.6 GHz several orders larger than that at 7.6 GHz. The weak intensity is because of a larger dielectric loss in lower bands and thus most energy is consumed in the prism, making the energy of a detected refractive wave relative small. At 8.2 GHz, very evident negative refraction is observed and the refracted angle is calculated as $\theta_r = -4.4^\circ$. Therefore, the refractive index computed by $n = \sin\theta_r/\sin\theta_i$ is -0.13 according to Snell's law. Referring to Fig. 14(b), the refracted beam at 8.3 GHz is quasi-parallel to the direction normal to the tilted interface, illustrating that n extremely

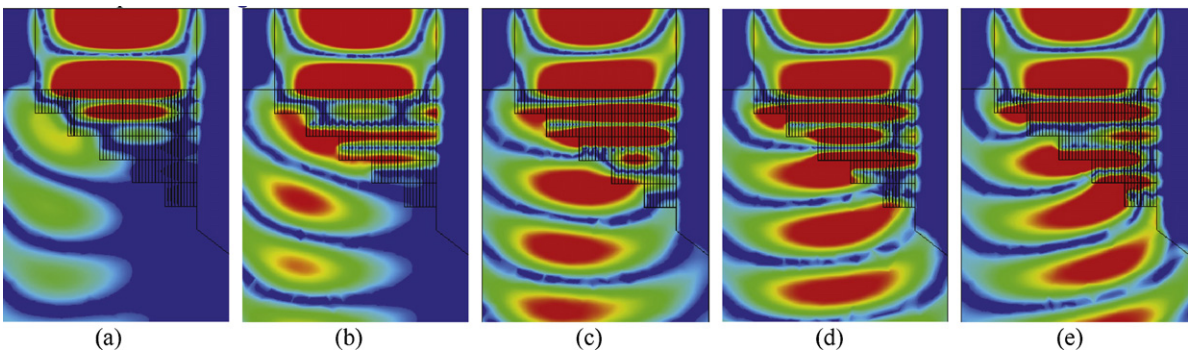

Fig. 14. Electric-field distributions of refracted beams at different frequencies in the fundamental composite passband. (a) 8.2 GHz, (b) 8.3 GHz, (c) 8.4 GHz, (d) 8.5 GHz, and (e) 8.6 GHz.

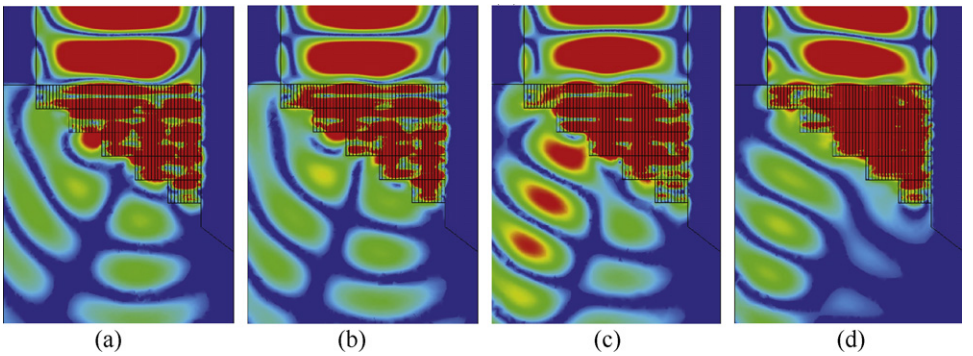

Fig. 15. Electric-field distributions of refracted beams at different frequencies in the second LH band. (a) 11 GHz, (b) 11.1 GHz, (c) 11.2 GHz, and (d) 11.3 GHz.

approximates to zero. At 8.4 GHz and residual frequencies, see from Fig. 14(c)–(e), the peak of the refractive beam is directed positive (RH behavior) with a gradually increased θ_r at higher frequencies. These frequencies of negative refraction coincide well with those depicted in Figs. 11 and 12.

To provide a complementary validation of the LH characteristic (negative refraction) in the second LH band identified in Fig. 3, the electric-field distribution of the same prism from 11 to 11.3 GHz is plotted in Fig. 15. The most striking physical phenomenon should be that there are two divisive reflected beams at former three frequencies while inversely the side lobe is mostly eliminated at the last frequency. The side lobe is induced partially by the diffraction effects due to the slightly large electric dimensions and partially by the mismatch of the prism to free space. On the other hand, the main beam refracts from the third tilted stair while the parasitical side lobe originates from the fourth tilted stair. The discrepancy of effective material parameters between LHMs that have different numbers of unit cells along propagation direction give rise to the divisive beams. Nevertheless, the negative refraction ambiguously dominates and the scan angle reduces with frequency within the observed frequency range, and does not occur outside this range. At 11 and 11.1 GHz, the main beam is directed negative with $\theta_r = -24.3^\circ$ and provides a negative index of -0.7, whereas at 11.2 and 11.3 GHz, θ_r is observed at -3.8° and Re(n) is calculated as -0.11.

4. Conclusion

In summary, a novel LHM inspired by tree-shaped fractal with multi-resonant electric and magnetic resonances have been numerically and experimentally studied. The identification of the multi resonances has been performed through the field analysis as well as the circuit model analysis. MB negative permittivity exhibits because the LHM cell embodies simultaneously a plasma response and a cut-wire electric resonance, whereas three magnetic resonances providing MB negative permeability are accounted by three current loops with modulated magnetic dipole moments formed in specified DSRs. A most striking characteristic should be the robust magnetic resonances and the fundamental balanced passband which always exhibit no matter how lattice constants vary. The LH behavior has been validated by both a prism and a slab. The avenue of realizing LHMs using commercially available standard printed circuit board technique has practical values in designing planar MB LHMs, advancing a step in this area.

Acknowledgements

This work is supported by the National Natural Science Foundation of China under Grant No. 60971118 and the 973 Project of Science and Technology Ministry under Grant No. 2009CB613306. The authors would like to thank anonymous reviewers for their constructive comments and China North Electronic Engineering Research Institute for the fabrication.

References

[1] V.G. Veselago, Soviet Physics Uspekhi 10 (1968) 509.
[2] R.A. Shelby, D.R. Smith, S. Schultz, Science 292 (2001) 77–79.
[3] J.B. Pendry, A.J. Holden, D.J. Robbins, W.J. Stewart, IEEE Transactions on Microwave Theory and Techniques 47 (1999) 2075.
[4] J.B. Pendry, A.J. Holden, W.J. Stewart, I. Youngs, Physical Review Letters 76 (1996) 4773.
[5] J.T. Huangfu, L.X. Ran, H.S. Chen, X.M. Zhang, K.S. Chen, T.M. Grzegorczyk, J.A. Kong, Applied Physics Letters 84 (2004) 1537.

[6] F. Zhang, G. Houzet, E. Lheurette, D. Lippens, M. Chaubet, X. Zhao, Journal of Applied Physics 103 (2008) 084312.
[7] J. Zhou, T. Koschny, L. Zhang, G. Tuttle, C.M. Soukoulis, Applied Physics Letters 88 (2006) 221103.
[8] J. Zhou, L. Zhang, G. Tuttle, Th. Koschny, C.M. Soukoulis, Physical Review B 73 (2006), 041101(R).
[9] M. Kafesaki, I. Tsiapa, N. Katsarakis, Th. Koschny, C.M. Soukoulis, E.N. Economou, Physical Review B 75 (2007) 235114.
[10] J. Wang, S. Qu, Z. Xu, H. Ma, S. Xia, Y. Yang, X. Wu, Q. Wang, C. Chen, Physical Review E 81 (2010) 036601.
[11] Y. Yao, X.P. Zhao, Journal of Applied Physics 101 (2007) 124904.
[12] R. Liu, A. Degiron, J.J. Mock, D.R. Smith, Applied Physics Letters 90 (2007) 263504.
[13] H. Chen, L. Ran, J. Huangfu, X. Zhang, K. Chen, Physical Review E 70 (2004) 057605.
[14] H.-X. Xu, G.-M. Wang, Q. Liu, J.-F. Wang, J.-Q. Gong, Applied Physics A 107 (2012) 261.
[15] J. Wang, S. Qu, Y. Yang, H. Ma, X. Wu, Z. Xu, Applied Physics Letters 95 (2009) 014105.
[16] D.-H. Kwon, D.H. Werner, A.V. Kildishev, V.M. Shalaev, Optics Express 15 (2007) 1647.
[17] Q. Du, J. Liu, H. Yang, X. Yi, Applied Optics 50 (2011) 4798.
[18] G. Dolling, C. Enkrich, M. Wegener, J.F. Zhou, C.M. Soukoulis, S. Linden, Optics Letters 30 (2005) 3198.
[19] T. Driscoll, G.O. Andreev, D.N. Basov, S. Palit, S.Y. Cho, N.M. Jokerst, D.R. Smith, Applied Physics Letters 91 (2007) 062511.
[20] N. Liu, H.C. Guo, L.W. Fu, S. Kaiser, H. Schweizer, H. Giessen, Nature Materials 7 (2008) 31.
[21] J. Valentine, S. Zhang, T. Zentgraf, E. Ulin-Avila, D.A. Genov, G. Bartal, X. Zhang, Nature (London) 455 (2008) 376.
[22] D. Schurig, J.J. Mock, B.J. Justice, S.A. Cummer, J.B. Pendry, A.F. Starr, D.R. Smith, Science 314 (2006) 977.
[23] R. Liu, C. Ji, J.J. Mock, J.Y. Chin, T.J. Cui, D.R. Smith, Science 323 (2009) 366.
[24] E. Semouchkina, D.H. Werner, G.B. Semouchkin, C. Pantano, Applied Physics Letters 96 (2010) 233503.
[25] J.B. Pendry, D.R. Smith, Scientific American 295 (2006) 60.
[26] J. Zhao, Y. Feng, B. Zhu, T. Jiang, Optics Express 16 (2008) 18057.
[27] N.I. Landy, S. Sajuyigbe, J.J. Mock, D.R. Smith, W.J. Padilla, Physical Review Letters 100 (2008) 2074021.
[28] X.-J. He, Y. Wang, J.-M. Wang, T.-L. Gui, Progress in Electromagnetics Research 115 (2011) 381.
[29] J. McVay, N. Engheta, A. Hoorfar, Proc. IEEE AP-S Int. Symp. Antennas Propag., 2005, p. 328.
[30] W. Wen, L. Zhou, B. Hou, C.T. Chan, P. Sheng, Physical Review B 72 (2005) 153406.
[31] F. Miyamaru, Y. Saito, M.W. Takeda, B. Hou, L. Liu, W. Wen, P. Sheng, Physical Review B 77 (2008) 045124.
[32] J.M. Hao, L. Zhou, C.T. Chan, Applied Physics A 87 (2007) 281.
[33] L. Yousefi, O.M. Ramahi, IEEE Transactions on Antennas and Propagation 58 (2010) 2614.
[34] H.-X. Xu, G.-M. Wang, J.-G. Liang, Radio Science 46 (2011) RS5008.
[35] T. Koschny, P. Markos, D.R. Smith, C.M. Soukoulis, Physical Review E 68 (2003) 065602.
[36] D.H. Werner, A. Rubio Bretones, B.R. Long, Electronics Letters 35 (1999) 609.
[37] K. Aydin, Z. Li, S. Bilge, Photonics and Nanostructures: Fundamentals and Applications 6 (2008) 116.
[38] X.D. Chen, T.M. Grzegorczyk, B.-I. Wu, J. Pacheco Jr., J.A. Kong, Physical Review E 70 (2004) 016608.
[39] D.R. Smith, D.C. Vier, Th. Koschny, C.M. Soukoulis, Physical Review E 71 (2005) 036617.
[40] Z. Li, K. Aydin, E. Ozbay, Physical Review E 79 (2009) 026610.
[41] F. Urbani, IEEE Antennas and Wireless Propagation Letters 9 (2010) 720–723.
[42] H. Chen, L. Ran, J. Huangfu., G. Grzegorczyk, J.A. Kong, Journal of Applied Physics 100 (2006) 024915.
[43] T. Koschny, P. Markos, E.N. Economou, D.R. Smith, D.C. Vier, C.M. Soukoulis, Physical Review B 71 (2005) 245105.
[44] J. Zhou, T. Koschny, M. Kafesaki, C.M. Soukoulis, Size dependence and convergence of the retrieval parameters of metamaterials, Photonics and Nanostructures: Fundamentals and Applications 6 (2008) 96.